Traveling wave profiles for a crystalline front invading liquid states: analytical and numerical solutions

P. K. Galenko[a,b,*], F. Iunes Sanches[c], K. R. Elder[c]

[a] *Friedrich-Schiller-Universität Jena, Physikalisch-Astronomische Fakultät, D-07743 Jena, Germany*
[b] *Ural Federal University, Laboratory of Multi-Scale Mathematical Modeling, 620002 Ekaterinburg, Russla*
[c] *Department of Physics, Oakland University, Rochester, MI, 48309-4487, USA*

Abstract

The properties of a two dimensional crystalline phase invading a metastable or unstable liquid state are examined using the amplitude expansion formulation of the hyperbolic and parabolic phase-field crystal model. When the amplitudes are real and equal to each other, analytic expressions are derived for the profile of a steady state liquid-solid front traveling at constant velocity. Numerical simulations of the full amplitude formulation are conducted and compared with the analytic results. Close to the melting transition the analytic results for the liquid-solid profile, velocity and width are in quantitative agreement with the numerical results and disagree far from the transition.

Keywords: Crystal, Model, Pattern Selection, Travelling Wave

*Corresponding author
Email address: peter.galenko@uni-jena.de (P. K. Galenko)

1. Introduction

When phase transformations occur it is often the case that interfaces or domain walls form between different phases or states. The interaction and motion of these interfaces play a key role in the subsequent evolution of the system. For example, in order-disorder transitions domain walls form between different, but energetically equivalent, variants of a given sublattice ordering. Subsequent evolution towards equilibrium is then thought to be driven by the curvature of the domain walls [1]. One reason that many studies [2, 3, 4] have been devoted to understand the dynamics and motion of such domain walls is that the motion often leads to complex spatial structures which strongly influence material properties. For example, properties such as the yield strength and magnetic coercivity are known to be a strong function of grain size in polycrystalline materials [5]. Another interesting aspect of interface motion is that when a stable phase invades a metastable or unstable phase it is possible that the state that is selected at the front is not exactly the equilibrium state as occurs when a periodic phase invades a uniform state. In this instance, the periodicity that is selected near the propagating front may not be the equilibrium periodicity. This could potentially lead to a strained state or in extreme circumstances a glassy state [6].

Recently, the phase field crystal (PFC) model has been used to examine the dynamics of liquid-solid, grain boundaries and dislocation motion [7, 8, 9, 10]. The PFC model is a continuum model that describes processes on atomic length scales and patterns on the nano- and micro-length scales [10, 11]. This model is characterized by a free energy that is a functional of a field (n) that is periodic in the solid phase and uniform in a liquid state and an equation of motion that conserves the average value of n. The periodicity of n naturally incorporates elasticity and multiple crystal orientation which allows the model to be used to study a number of phenomena including epitaxial growth, ordering of nano-scale structures on micron length scales [11], liquid-solid transitions, dislocation motion and plasticity, glass formation and foams, grain boundary premelting, crack propagation, surface reconstructions, grain boundary energies, dynamics of colloidal systems and polymers (see overview [12] and references therein).

In a previous work the selection of a periodic state as it invades an unstable state was examined in the one-dimensional PFC-model with both hyperbolic and parabolic dynamics [6]. A marginal stability analysis was used to determine the velocity and periodicity of the front. It was found that the

periodicity of the selected state was different from the equilibrium state and as expected did depend on the type of dynamics. For very high driving forces it was also found that the periodicity selected was above the Eckhaus instability leading to the speculation of glassy states. The results of the work [6] were quantitatively verified with direct numerical simulations [13].

In this work we consider the solidification of a crystalline state from a metastable or unstable liquid state as described by the two-dimensional PFC model and develop analytic solutions for a crystalline front invading the liquid. Here we assume that the transition from the metastable state to the stable state occurs by overcoming the energy barrier which is usually necessary for the emergence of a new phase. Contrary to that, the transition from the unstable state proceeds without energetic barrier that is usually evolves by fluctuation mechanism. The analysis of these two transitions is based on the amplitude representation of the PFC model [14, 15] in which the conserved scalar field n is represented by a set of complex amplitudes that are assumed to vary on length scales larger than the wavelength of n. The phase of the amplitudes allows for elastic strains and multiple crystal orientation and the magnitude of the amplitudes incorporates liquid-solid interfaces and transitions. The combination of the phase and magnitude allows for more complex features such as dislocations and grain boundaries. However, some features, such as Peierls barriers and faceting are missing from the amplitude description used in this work, although higher order corrections are possible [16]. In this paper analytic solutions for a crystalline front invading an unstable and metastable liquid state are derived in the limit in which the amplitude can be represented by a single magnitude only. For comparison, numerical simulations of the full amplitude description are also conducted.

The paper is organized as follows. Section 2 presents a formulation of the model which introduces governing hyperbolic PFC-equation. This equation describes simultaneously dissipation for diffusive regimes existing in slow transitions and inertia for propagative regimes occurring in fast phase transitions. In Section 3, the amplitude equations are first introduced and then simplified to a magnitude (ϕ) only description. In Section 4 the equilibrium properties of the system are described in terms of ϕ. The dynamics and traveling wave solution for the real amplitude of the triangular pattern propagating into unstable and metastable homogeneous states are obtained. In Section 5, numerical solutions of the full amplitude formalism are presented and compared with the analytic solutions. Conclusions are given in Section 6. Appendix A presents details of analytical method based on amplitude wave

representation. Appendix B gives details of the computational scheme used in the numerical modeling. Finally, Appendix C describes numerical estimations for the relaxation times used in the presented model.

2. Hyperbolic PFC-model

The hyperbolic PFC model describes a first order liquid-solid transformation in terms of a field, $n(\vec{r},t)$, that is related to the dimensionless local atomic number density and a flux $\vec{J}(\vec{r},t)$. The free energy functional [6, 17] is a functional of n and $\vec{J}$ and can be written in dimensionless form as

$$\mathcal{F}[n,\vec{J}] = \mathcal{F}_{eq}[n] + \mathcal{F}_{neq}[\vec{J}]. \tag{1}$$

The local equilibrium contribution is given by [20]

$$\mathcal{F}_{eq} = \int \left[\frac{n}{2}\mathcal{L}\, n - \frac{a}{3}n^3 + \frac{v}{4}n^4\right] d\vec{r}, \tag{2}$$

where

$$\mathcal{L} \equiv \Delta B_0 + B_0^x(1 + 2R_o^2\nabla^2)^2. \tag{3}$$

ΔB_0, B_0^x, R_o, a and v are phenomenological parameters that can be fit to various physical properties of the systems as discussed in references [18, 19, 20, 21]. Briefly the sum, $B_0^\ell = \Delta B_0 + B_0^x$, is the dimensionless liquid state compressibility, B_0^x is proportional to the elastic moduli, R_o sets the length scale of the lattice and a and v determine the magnitude of the fluctuations in the solid state and the size of the miscibility gap in n at liquid-solid coexistence. The free energy functional (2) describes a transition from a liquid state (n = constant) at high ΔB_0 to a crystalline state (n = periodic) at low or negative values of ΔB_0 [20, 21]. In this respect, the parameter ΔB_0 can be thought of as a control parameter similar to a temperature difference.

The nonequilibrium contribution is given by

$$\mathcal{F}_{neq}[\vec{J}] = \frac{\tau}{2}\int \vec{J}\cdot\vec{J}\, d\vec{r}, \qquad \tau > 0, \tag{4}$$

where τ is the characteristic time for relaxation of the flux $\vec{J}$ to its steady state. The dynamics are described by a continuity equation to ensure conservation of n, i.e.,

$$\frac{\partial n}{\partial t} + \vec{\nabla}\cdot\vec{J} = 0. \tag{5}$$

The non-equilibrium contribution to energy (4) is introduced phenomenologically by the extended thermodynamics [22] or by the generalized hydrodynamics [23]. The requirement that the free energy given in Eq. (1) decreases (or is constant) in time leads to the hyperbolic equation [17, 24]:

$$\tau\frac{\partial^2 n}{\partial t^2}+\frac{\partial n}{\partial t}=\nabla^2\left[\mathcal{L}n-an^2+vn^3\right]. \tag{6}$$

The hyperbolic phase-field equation (6) contains both the relaxation of slow conserved variable $n(\vec{r},t)$ and fast non-conserved variable $\vec{J}(\vec{r},t)$ to their own steady-states (see Ref. [22] and references therein). As a result of these two relaxation processes, Eq. (6) shows that, in addition to the dissipation described by the traditional parabolic PFC-equation [7], inertia $\propto \partial^2 n/\partial t^2$ is also taken into account due to kinetic contribution (4). Alternatively, Eq. (6) was proposed by Stefanovic et al. [25, 26] to incorporate both fast elastic relaxation and slower mass diffusion. Similar equations have also been obtained using dynamical density functional theory by Archer [27]. As a result, Eq. (6) can describe the dynamics of a periodic crystalline state invading a metastable or unstable liquid state and vice versa. To obtain an understanding of these processes an analytic solution will be derived by considering an amplitude representation of Eq. (6) as described in the next section.

3. Amplitude's equation

For mathematical convenience it is useful to write the solutions of the atomic density n in terms of the following expansion

$$\begin{aligned} n &= n_o+\sum_{klm}\eta_{klm}\exp\left(i\vec{G}_{klm}\cdot\vec{r}\right)+\sum_{klm}\eta^*_{klm}\exp\left(-i\vec{G}_{klm}\cdot\vec{r}\right) \\ &\equiv n_o+\sum_{j=1}^{3}\left[\eta_{klm}\exp\left(i\vec{G}_{klm}\cdot\vec{r}\right)+\text{c.c.}\right], \end{aligned} \tag{7}$$

where the small-scale crystalline structure is characterized by the vectorial factor

$$\vec{G}_{klm}=k\vec{q}_1+l\vec{q}_2+m\vec{q}_3, \tag{8}$$

which is needed to reconstruct the lowest order wavevectors of a given symmetry. $(\vec{q}_1,\vec{q}_2,\vec{q}_3)$ are the principle reciprocal lattice vectors, the integers

(k,l,m) are the Miller indices, η_{klm} is a complex amplitude, η^*_{klm} is the complex conjugate of η_{klm}, n_o is the average density and "c.c." refers to the complex conjugate. In principle, a density difference between the liquid and solid states should exist, but for the purposes of this work n_o will be assumed to a constant. To obtain an exact match to the equilibrium solutions all integer values of (k,l,m) must be used, however close to the liquid-solid transition, it is a good approximation for the PFC model to include only the lowest order terms.

We consider a two-dimensional system in which the crystalline state has triangular symmetry with lattice parameter q and principle reciprocal lattice vectors $\vec{q}_1 = -q(\sqrt{3}/2\hat{i}_1 + 1/2\hat{i}_2)$, $\vec{q}_2 = q\hat{i}_2$ and $\vec{q}_3 = \vec{0}$ (where $\hat{i}_1$ and $\hat{i}_2$ are unit vectors and we note only two vectors are needed in two dimensions). Near the transition it is sufficient to consider three amplitudes corresponding to $(k,l,m) = (1,0,0), (0,1,0), (\bar{1},\bar{1},0)$, where using standard notation [28] the $\bar{k} \equiv -k$ for example. As has been done in prior publications [10, 20] it is convenient to refer to these vectors as simply $\vec{G}_1 \equiv \vec{G}_{100}$, $\vec{G}_2 \equiv \vec{G}_{010}$ and $\vec{G}_3 \equiv \vec{G}_{\bar{1}\bar{1}0}$, and similarly with the amplitudes, i.e., $\eta_{100} \equiv \eta_1$, $\eta_{010} \equiv \eta_2$ and $\eta_{\bar{1}\bar{1}0} \equiv \eta_3$. To derive equations of motion for the amplitudes we also consider the length scale over with they vary is much larger than the lattice spacing. The magnitude of the amplitudes is constant in a perfect crystalline state and go to zero in the liquid state (as shown in Fig. 1) or near grain boundaries. As a result, the equations of motion for the corresponding amplitudes can be derived by integrating over one unit cell and assuming that the amplitudes are constant on these length scales [14, 20, 21, 29]. The equations of motion become (see, for details, Appendix A)

$$\left(\tau\frac{\partial^2}{\partial t^2} + \frac{\partial}{\partial t}\right)\eta_j = -\left(\Delta B_0 + B_0^x \mathcal{G}_j^2\right)\eta_j$$
$$+2a\prod_{m\neq j}\eta_m^* - 3v\left(A_\eta^2 - |\eta_j|^2\right)\eta_j, \qquad A_\eta^2 = 2\sum_{j=1}^{3}|\eta_j|^2, \tag{9}$$

where the operator $\mathcal{G}_j$ is given by

$$\mathcal{G}_j = \nabla^2 + 2i\vec{G}_j\cdot\vec{\nabla} + 1 - q^2, \quad with \;\; j = 1,2,3. \tag{10}$$

For convenience all length scales have been scaled by R_o so that in the equilibrium state the magnitude of wave-number q is unity. The amplitude equations (9) are similar to those obtained in Ref. [11] in that the expansion is

about a strained state, which leads to a modification of the operator (10) by the $1-q^2$ term in comparison with other expansions [14, 20, 21] which do not contain this term. Namely, the term $1-q^2$ arises in Eq. (10) from expanding the amplitude function around a wave-number different from the equilibrium value of 1 as is done in references [14, 20, 21], but not in reference [11]. More explicitly, when $\vec{G}_1$, $\vec{G}_2$ and $\vec{G}_3$ are given by $-q(\sqrt{3}/2\hat{i}_1 + 1/2\hat{i}_2)$, $q\hat{i}_2$ and $q(\sqrt{3}/2\hat{i}_1 - 1/2\hat{i}_2)$, respectively, instead of the equilibrium wave-numbers, $q = 1$, then this extra term appears if the Laplacian operates on the atomic density n, i.e.,

$$\nabla^2 n = \sum_{j=1}^{3} e^{i\vec{G}_j\cdot\vec{r}} \left(\nabla^2 + 2i\vec{G}_j\cdot\vec{\nabla} + 1 - q_j^2\right)\eta_j, \quad with \quad j = 1, 2, 3.$$

This leads to the origin of the extra term in Eq. (9). Obviously, with $q_j = 1$, the Laplacian transforms to $\nabla^2 + 2i\vec{G}_j\cdot\vec{\nabla}$ as in Refs. [14, 20, 21] (with no extra term in Eq. (9)).

The amplitude equations (9) can be written in a modified Allen-Cahn form [22], i.e.,

$$\tau\frac{\partial^2\eta_j}{\partial t^2} + \frac{\partial\eta_j}{\partial t} = -\frac{\delta\mathcal{F}_\eta}{\delta\eta_j^*}, \tag{11}$$

in which the free energy is described as

$$\mathcal{F}_\eta = \int d\vec{r}\Bigg[\frac{\Delta B_0}{2}A_\eta^2 + \frac{3v}{4}A_\eta^4 - 2a\left(\prod_{j=1}^{3}\eta_j + c.c.\right) + \sum_{j=1}^{3}\left\{B_0^x|\mathcal{G}_j\eta_j|^2 - \frac{3v}{2}|\eta_j|^4\right\}\Bigg]. \tag{12}$$

We note that in the limit of small value of ΔB_0 in the PFC-model the equilibrium value of $q = q_e$ is only 1 for when $\Delta B_0 = 0$. However, in the amplitude model described above the free energy functional (12) is minimized by $q = 1$ exactly, since only the lowest order modes were included.

To make further progress we consider the limit in which all the amplitudes are real and identical, that is we represent $\eta_j \approx \phi$ for all j. In this instance it is possible to obtain an analytic solution for a traveling wave front describing a crystal state invading a supercooled liquid (or a liquid phase invading a

superheated crystal state). One can show that the sum of the three amplitude equations given by Eq. (9) reduces to the following equation

$$\left(\tau\frac{\partial^2}{\partial t^2}+\frac{\partial}{\partial t}\right)\phi=-\Delta B_0\phi-\frac{B_0^x}{3}\sum_{j=1}^{3}\mathcal{G}_j^2\phi+2a\phi^2-15\phi^3, \tag{13}$$

in which we have assumed $\phi=\eta_1=\eta_2=\eta_3$ (see also Ref. [10]). In order to proceed we will make a long-wavelength approximation and assume that the ∇^2 term can be neglected in $\mathcal{G}_j$, to obtain,

$$\sum_{j=1}^{3}\mathcal{G}_j^2\phi\approx\sum_{j=1}^{3}\left\{-4q^2(\vec{G}_j\cdot\vec{\nabla})^2+i2q(1-q^2)\vec{G}_j\cdot\vec{\nabla}\right\}\phi+3(1-q^2)^2\phi. \tag{14}$$

Without further approximation one can perform the summations and obtain the result

$$\sum_{j=1}^{3}\mathcal{G}_j^2\phi\approx-6q^2\nabla^2\phi+3(1-q^2)^2\phi. \tag{15}$$

Substituting Eq. (15) into Eq. (13) gives the following amplitude equation:

$$\left(\tau\frac{\partial^2}{\partial t^2}+\frac{\partial}{\partial t}\right)\phi=2B_0^xq^2\nabla^2\phi-\Delta\tilde{B}_0\phi+2a\phi^2-15v\phi^3, \tag{16}$$

where we introduced

$$\Delta\tilde{B}_0=\Delta B_0+(1-q^2)^2B_0^x. \tag{17}$$

This can also be re-written as

$$\left(\tau\frac{\partial^2}{\partial t^2}+\frac{\partial}{\partial t}\right)\phi=-\frac{\delta F_\phi}{\delta\phi}, \tag{18}$$

where

$$F_\phi\equiv\int d\vec{r}\left(\Delta\tilde{B}_0\frac{\phi^2}{2}-2a\frac{\phi^3}{3}+15v\frac{\phi^4}{4}+B_0^xq^2|\vec{\nabla}\phi|^2\right). \tag{19}$$

Equation (16) describes evolution of the amplitudes of the periodic triangular pattern described by the PFC model in the long-wave limit. The

field $\phi = |\eta_{\vec{G}}|$ is the envelope of the periodic triangular pattern and can be thought as the phase field variable used to describe the liquid-solid transition (as is shown in Fig. 1). Our calculations show that the ϕ-field satisfies a non-conserved hyperbolic Allen-Cahn type equation (11) [or Eq. (18)]. One interesting feature of this result is that the parameter $\Delta\tilde{B}_0$ is always greater than ΔB_0 when q is not the equilibrium value (i.e., $q \neq 1$). This implies an effectively higher temperature which should slow down a solid front invading a liquid state, if the solid is strained.

Equation (16) and expression (17) describe the transition from a metastable state which occurs if the compressibility B_0^ℓ is greater than the elastic modulus B_0^x, such that $\Delta B_0 \equiv B_0^\ell - B_0^x > 0$. Another situation may exist if the compressibility B_0^ℓ becomes smaller than the elastic modulus B_0^x, $\Delta B_0 \equiv B_0^\ell - B_0^x < 0$, giving an unstable state for the system. In the latter case, it is straightforward to show that, in analogy with the above analytical treatments, the transition from unstable state is described by

$$\left(\tau\frac{\partial^2}{\partial t^2} + \frac{\partial}{\partial t}\right)\phi = 2B_0^x q^2\nabla^2\phi + |\Delta\tilde{B}_0|\phi + 2a\phi^2 - 15v\phi^3, \tag{20}$$

with

$$|\Delta\tilde{B}_0| = |\Delta B_0| + (1-q^2)^2 B_0^x. \tag{21}$$

Equations (17) and (21) take into account expansion for arbitrary values of the wave-number q selected at the front of a periodic pattern invading a metastable phase or unstable phase, respectively.

4. Transition from metastable and unstable states

4.1. Free energy density

When a liquid is quenched just below the melting temperature it is usually the case that a solid phase nucleates and then invades the metastable supercooled liquid, as typically occurs in first order phase transitions. Of course, if the liquid is quenched far below the transition temperature the liquid can become unstable as opposed to metastable and there exists the possibility of the crystalline state invading an unstable liquid phase.

In the following analysis, we shall distinguish between transitions from metastable or unstable states through the standard thermodynamic description of the homogeneous part of the free energy density. With this aim, we

consider the properties of the free energy given in Eq. (19) with $|\vec{\nabla}\phi| = 0$ described below and shown in Fig. 2:

(*i*) For $\Delta\tilde{B}_0 > 8a^2/(135v)$, the homogeneous high-temperature liquid state (i.e., $\phi = 0$) is the lowest energy state. In this state the solid state is metastable if $8a^2/(135v) < \Delta\tilde{B}_0 < a^2/(15v)$ and unstable if $\Delta\tilde{B}_0 > a^2/(15v)$.

(*ii*) The liquid and solid states have the same energy at $\Delta\tilde{B}_0 = 8a^2/(135v)$ which would correspond to the melting temperature.

(*iii*) In the range $0 < \Delta\tilde{B}_0 < 8a^2/(135v)$ the solid has the lowest energy and the liquid is in a metastable state. A fluctuation mechanism or external trigger is required for the system to solidify if the initial state is in the liquid, $\phi = 0$, state.

(*iv*) The spinodal occurs when $\Delta\tilde{B}_0 = 0$ and the liquid is linearly unstable to the formation of the lowest energy solid phase when $\Delta\tilde{B}_0 < 0$.

4.2. Traveling wave solutions

Consider a periodic crystalline state invading the homogeneous liquid state. Transformation from an unstable liquid phase occurs for the condition $\Delta\tilde{B}_0 < 0$, which energetically corresponds to all possible curves lying below the bottom curve in Fig. 2. The transition from a metastable state usually occurs near first order transitions as in the classical example of solidification from an undercooled liquid. In this case, transformation occurs for the condition $\Delta\tilde{B}_0 > 0$, which energetically corresponds to all possible curves lying above the bottom curve up to the curve given by the condition $\Delta\tilde{B}_0 = 8a^2/(15v)$ corresponding to phase coexistence, Fig. 2. Both transitions can be analyzed by unified solution of Eqs. (16) and (20).

For the analysis, it is convenient to introduce the following parameters

$$\begin{aligned}
&\zeta = q\sqrt{2B_0^x/|\Delta\tilde{B}_0|}, \quad t_0 = |\Delta\tilde{B}_0|^{-1}, \\
&V_0 = \zeta/t_0 = q\sqrt{2B_0^x|\Delta\tilde{B}_0|}, \\
&\phi_0 = \sqrt{|\Delta\tilde{B}_0|/(15v)}.
\end{aligned} \tag{22}$$

Note that all the above parameters are a function of $\Delta\tilde{B}$ which is a function of the dimensionless crystal wave-number q (in equilibrium value, $q = 1$), i.e., a function of the strain in the system. Now, using the scales (22), one can introduce variables

$$\tilde{t} = t/t_0, \quad \tilde{\vec{\nabla}} = \zeta^{-1}\vec{\nabla}, \quad \psi = \phi/\phi_0, \quad \tilde{x} = \zeta^{-1}x. \tag{23}$$

Taking into account these new scales and variables, Eqs. (16), (17), (20) and (21) can now be written in the following unified form

$$\frac{\tau}{t_0}\frac{\partial^2\psi}{\partial\tilde{t}^2}+\frac{\partial\psi}{\partial\tilde{t}}=\tilde{\nabla}^2\psi-\kappa_0\psi+\tilde{b}\psi^2-\psi^3, \tag{24}$$

where $\kappa_0=+1$ for $\Delta\tilde{B}_0>0$ (metastable), $\kappa_0=-1$ for $\Delta\tilde{B}_0<0$ (unstable), and $\tilde{b}$ is defined to be

$$\tilde{b}=\frac{2a}{\sqrt{15v|\Delta\tilde{B}_0|}}. \tag{25}$$

When the two states have equal energy $\Delta\tilde{B}_0=8a^2/135v$ one gets $\tilde{b}=3/\sqrt{2}$. Thus we expect that the velocity of the front will be zero at this value of $\tilde{b}$.

We now consider a steady state front propagating at a constant velocity V. In the moving coordinate frame Eq. (24) transforms to

$$\left(1-\frac{\tilde{V}^2}{\tilde{V}_\phi^2}\right)\frac{d^2\psi}{du^2}+\tilde{V}\frac{d\psi}{du}-\kappa_0\psi+\tilde{b}\psi^2-\psi^3=0, \tag{26}$$

where

$$\begin{aligned} &u=\tilde{x}-\tilde{V}\tilde{t},\quad \tilde{V}=V/V_0,\\ &\tilde{V}_\phi=\sqrt{t_0/\tau}=(|\Delta\tilde{B}_0|\tau)^{-1/2}=V_\phi/V_0, \end{aligned} \tag{27}$$

with $\tilde{V}_\phi$ the dimensionless parameter of the maximum speed V_ϕ for the perturbations propagation in the field of amplitude ϕ. Note that the scaling (27) is chosen to get the material parameter V_ϕ independent from the governing parameter $|\Delta B_0|$ such that: $V_\phi=\tilde{V}_\phi V_0=q\sqrt{2B_0^x/\tau}$.

Assuming constant values of the order parameter far from the front, $\psi=0$ at $u\to\infty$ and $\psi=1$ at $u\to-\infty$, a solution of Eq. (26) of the kink-form,

$$\psi(u)=A\left[1-\tanh(u/Z)\right], \tag{28}$$

can be found. Substituting this general solution into Eq. (26) and setting the coefficients of each powers of ψ equal to zero leads to the following system of equations

$$\begin{cases} A^2Z^2=2\left(1-\tilde{V}^2/\tilde{V}_\phi^2\right),\\ \tilde{b}AZ^2+\tilde{V}Z=6\left(1-\tilde{V}^2/\tilde{V}_\phi^2\right),\\ \kappa_0Z^2+2\tilde{V}Z=4\left(1-\tilde{V}^2/\tilde{V}_\phi^2\right). \end{cases} \tag{29}$$

Equations (29) give the solution for the amplitude-factor A,

$$A = \frac{\sqrt{2}}{6}(\tilde{b}\sqrt{2} + \tilde{V}_m) = \frac{1}{4}\left(\tilde{b} + \sqrt{\tilde{b}^2 - 4\kappa_0}\ \right), \tag{30}$$

the self-consistent velocity,

$$\tilde{V} = \frac{\tilde{V}_m}{\sqrt{1 + \tilde{V}_m^2/\tilde{V}_\phi^2}}, \tag{31}$$

with its maximum value, $\tilde{V}_m$, given by

$$\tilde{V}_m = \frac{\sqrt{2}}{4}\left(3\sqrt{\tilde{b}^2 - 4\kappa_0} - \tilde{b}\right), \tag{32}$$

and, finally, the correlation length

$$\begin{aligned} Z &= \frac{4\sqrt{2(1 - \tilde{V}^2/\tilde{V}_\phi^2)}}{\tilde{b} + \sqrt{\tilde{b}^2 - 4\kappa_0}} \\ &= \frac{4\sqrt{2}}{\left(\tilde{b} + \sqrt{\tilde{b}^2 - 4\kappa_0}\ \right)\sqrt{1 + \tilde{V}_m^2/\tilde{V}_\phi^2}}. \end{aligned} \tag{33}$$

The traveling wave solutions (28) with Eqs. (30)-(33) contain some interesting features. *Firstly*, from Eq. (33) it can be seen that when $\tilde{V}$ is large the thickness of the diffuse interface decreases. Eq. (33) together with Eq. (27) shows that a drastic shrinking of the interface ($Z \to 0$) may occur if the velocity V approaches to or merely comparable with the speed V_ϕ of the atomic disturbance propagation. *Secondly*, it can be seen that around the transition point (around the melting temperature), i.e. at $\tilde{b} \approx 3/\sqrt{2}$, the solutions become independent from the speed $\tilde{V}_\phi = (|\Delta\tilde{B}_0|\tau)^{-1/2}$ of the atomic disturbance propagation and the relaxation time τ of the atomic flux. Indeed, Eqs. (30)-(33) tend to $A \to \sqrt{2}/2$, $\tilde{V} \to 0$, $\tilde{V}_m \to 0$, and $Z \to 2$ with $\tilde{b} \to 3/\sqrt{2}$ and $\kappa_0 = +1$. This implies that the parabolic dynamics (or assumption of local-equilibrium dynamics) become valid close to the transition point. *Finally*, exactly at the transition point, a full static equilibrium exists in which: $q = 1$, $\tilde{V} = 0$, and $\tilde{V}_m = 0$ with $\tilde{b} \equiv b = 3/\sqrt{2}$. As expected, the velocity is zero at the melting temperature and the ψ-profile (28) becomes

stationary in the form: $\psi(\tilde{x}) = 2\sqrt{2}[1 - \tanh(\tilde{x}/2)]$. In the following section these predictions are compared with numerical simulations of the amplitude equations.

It is straightforward to extend the analysis and to obtain the analytical solution of the kink-form (28) to other dimensions and various patterns, since this only alters the value of the parameters in Eq. (26). For example, one can directly show that, propagation of stripes in the direction perpendicular to their geometrical axes can be reduced to a one-dimensional form in which the parameter $a = 0$ and, consequently, $\tilde{b} = 0$. In this particular case, the obtained parameters (30)-(33) for the kink-solution (28) of the equation (26) with $\kappa_0 = -1$ are given by

$$\begin{cases} A = \dfrac{1}{2}, \\ Z = \dfrac{2\sqrt{2}}{\sqrt{1 + \tilde{V}_m^2/\tilde{V}_\phi^2}}, \\ \tilde{V} = \dfrac{\tilde{V}_m}{\sqrt{1 + \tilde{V}_m^2/\tilde{V}_\phi^2}}, \quad with \;\; \tilde{V}_m = \dfrac{3\sqrt{2}}{2}. \end{cases} \tag{34}$$

Extensions to three-dimensional BCC-systems are also possible.

The results obtained depend on the governing parameter $|\Delta\tilde{B}_0|$ which is a function of the selected wave-number q. Thus, to obtain a complete theory, another selection rule would have to be derived to determine the value of q. For purposes of comparison with the full amplitude model we will simply use the equilibrium value $q = 1$. As will be shown in the next section this approximation is only good close to the melting temperature.

5. Numerical modeling: parameters, results and discussion

To test the validity of the calculations presented in the previous sections, numerical solutions of the amplitude equations were conducted for a two-dimensional triangular lattice invading metastable homogeneous state and vice versa. With this aim, the complex amplitudes were solved by Eqs. (9) using the numerical approximation presented in Appendix B. In these simulations the initial condition was a small crystalline solid seed (η_m finite) surrounded by a supercooled melt ($\eta_m = 0$). The solid front was propagating

in the x-direction. Boundary conditions for η_m were chosen as: periodic conditions at the ends of computational domain in the y-direction and constant values at the ends of computational domain in the x-direction.

To solve amplitude equations (9) the grid size is limited by the interfacial width (not by the atomic spacing as in the case of solving the equation (6) for the atomic density). It has been also taken into account that the amplitudes are constant in the y-direction, therefore, the calculations and results are independent of the width of interface between homogeneous and periodic states. As such, the simulations were merely done in two spatial dimensions on regular mesh with the size $\Delta x = \Delta y = 0.7$. To stabilize the solution of hyperbolic-type Eqs. (9), the time step has been chosen as $\Delta t = 0.001$ (as explained in Appendix B). Thirteen hundred grid points in the x direction were sufficient to obtain steady state front profiles. From these profiles the front velocity V and width Z were measured. For the calculations of the wave-number selected at the front in the steady state regime, it was necessary to use three thousand grid points. In the y-direction just four grid nodes were used, hence, the traveling front has been analyzed for a thin strip of material in quasi-one-dimensional space. In all simulations we have utilized the following numerical values: $B_0^x = a = 1$ and $v = 0.1$. Then, ΔB_0 was varied to obtain the different velocities, widths, and wave-numbers. A value of $q = 1$ was used for the operator in Eq. (10). In this instance variations in the phase of the amplitudes will evolve to take into account changes in the selected wave-number from this value. Each parameter range was then repeated for different values of the relaxation time τ taken in the present work as $\tau = 0$ and 0.1 (see estimation for τ and comments in Appendix C). To illustrate the nature of the traveling fronts a sample solution of equations (9) was used to reconstruct the density field, n using Eq. (7). This reconstruction is shown in Fig. 3 for parameters $\Delta B_0 - \Delta B_0^* = 0$ and $\tau = 0$.

Figures 4 and 5 show a comparison of the analytic results given by Eqs. (31)-(33) for the velocity and interfacial width, respectively, using $q = 1$. The results are plotted as function of driving force, $(\Delta B_0 - \Delta B_0^*)/\Delta B_0^*$, where the critical value $\Delta B_0^* = 8a^2/(135v) \approx 0.593$ corresponding to the parameter $b = 3/\sqrt{2}$. These figures show that the numerically calculated velocity V and interfacial width Z (points) qualitatively reproduce the analytical calculations (curves) for small values of the driving force. The best quantitative agreement of the numerical calculations with analytical predictions for V and Z is in the range, $-0.1 < (\Delta B_0 - \Delta B_0^*)/\Delta B_0^* < 0.1$. For instance, the interfacial width Z becomes sharper with the increase driving force (during

crystallization at $(\Delta B_0 - \Delta B_0^*)/\Delta B_0^* < 0$, Fig. 5) that is perfectly consistent with the PFC studies of crystal layer growth and pinning [16]. The disagreement between the numerical and analytic results at larger values of the driving force (Figs. 4 and 5) is likely due to the assumption that the selected wave-number is $q = 1$ and that the complex amplitudes can all be represented as a single real field, ϕ.

Figure 6 shows the difference δq between wave-number q, which was numerically calculated just behind the solidifying front and its equilibrium value q_e, i.e. $\delta q = q - q_e$, for $(\Delta B_0 - \Delta B_0^*)/\Delta B_0^* \leq 0$. For $(\Delta B_0 - \Delta B_0^*)/\Delta B_0^* > 0$, δq is always zero (as for a melting process). This figure shows that δq is a complex function of the driving force and difficult to predict. To the authors knowledge, rigorous analytic methods to determine the front velocity are not yet found.

A form of the interfacial profile between homogeneous undercooled liquid and perfectly periodic crystal is given analytically by the function of hyperbolic tangent [see Eq. (28) together with the parameters (30)-(33)]. This analytical profile was also compared with the numerical results. For this comparison, it should be noted that each amplitude η_j has both a magnitude (ϕ) and phase (θ). The relationship between strain and linear dependence of the phase on $\tilde{x}$ can be seen by considering the full expansion of density n with using Eq. (7) only for the real amplitude. If the phase of each amplitude is linear in $\tilde{x}$ (i.e. $\theta_j = \delta q \tilde{x}$) this is equivalent to changing the $\tilde{x}$-component $\left[\vec{G}\right]_{\tilde{x}}$ to $\left[\vec{G}\right]_{\tilde{x}} + \delta q$. Thus, for $j = 3$ it would give $(q_e + 2/\sqrt{3}\delta q)\sqrt{3}/2$ or an effective q of $q = 1 + 2/\sqrt{3}\delta q = 1 + 2/\sqrt{3} d\theta/d\tilde{x}$ since the equilibrium wave-number is $q = q_e = 1$. As a result, in regions where θ is a linear function of $\tilde{x}$ the derivative $d\theta/d\tilde{x}$ is a measure of the strain or change in wave-number. As a result, the slope $d\theta/d\tilde{x} = q - 1$ represents the difference between the bulk value of q and its equilibrium value $q_e = 1$. A comparison of the analytic and numerical results are given at equilibrium (Fig. 7) and at a driving force of $(\Delta B_0 - \Delta B_0^*)/\Delta B_0^* = -0.6$ for parabolic PFC-model with $\tau = 0$ and hyperbolic PFC-model with $\tau = 0.1$ (Figs. 8 and 9).

Figure 7 shows that the analytic ϕ-profile is reasonably close to the ϕ-profile obtained from the amplitude equations in the thermodynamic equilibrium. In the range of driving force around equilibrium one may also find well fit for the ϕ-profile obtained from the analytical and numerical solutions. As the velocity of the front increases the fits deviate from the analytically predicted profiles, Figs. 8 and 9. This result is consistent with the above

outcomes for V, Z and q.

Finally, the numerical and analytic calculations presented here show that for a given value of $\tau = 0.1$ there is a quantitative (but not qualitative) difference between parabolic and hyperbolic dynamics in a pure material. This difference is more pronounced for high negative values of the driving force $(\Delta B_0 - \Delta B_0^*)/\Delta B_0^*$, Figs. 4-6. The same outcome follows also from the solution of self-consistent problem for solidification from an undercooled one-component liquid [30]. This differs from the solidification of a binary alloy where solute trapping can quantitatively change the behavior as has been demonstrated previously [31, 32] and in very recent simulations of the binary PFC model [33].

6. Conclusions

A phase-field model with one-order parameter, ϕ, was obtained from the amplitude representation [14, 20, 21] of the hyperbolic PFC-equation (6) as described by Eq. (9). This order parameter represents the envelope of the periodic field n which is changed between phases by the amplitude ϕ. Analytic solutions for ϕ were derived for the case of a solid phase invading a homogeneous metastable or unstable phase with arbitrary driving force, $(\Delta B_0 - \Delta B_0^*)/\Delta B_0^*$. In the reference frame of the traveling front the solutions are of the form: $\phi = A[1 - \tanh(u/Z)]$, where $u = x - Vt$ is the spatial coordinate traveling with the constant front velocity V. To our knowledge these are the first analytical solutions for the PFC equation (hyperbolic or parabolic) for a solid front invading a metastable or unstable liquid.

At small values of the driving force, $-0.1 < (\Delta B_0 - \Delta B_0^*)/\Delta B_0^* < 0.1$, the analytic solutions provide a reasonably accurate description of the front. More specifically, predictions for the velocity V, interface width Z and profile $\phi(x - Vt)$ are in reasonable agreement with the numerical simulations of the full amplitude description. The numerical simulations also show that the wave-number q selected near the front is different from the equilibrium value for intermediate and large values of the driving force, $(\Delta B_0 - \Delta B_0^*)/\Delta B_0^*$. In order to provide a more accurate analytic description of the moving front a theoretical prediction for the selected wave-number would be needed in this regime. Finally, we note that the analysis provided in this work are easily applicable to systems with different crystal symmetries (as is given for FCC-,

BCC-, HCP-, etc. crystal primary structures[1] [20, 21]). It would also be interesting to extend this work to binary systems to investigate nonequilibrium effects such as solute trapping [34], disorder trapping [35], and degeneration of solute drag [36, 37] which appear at the rapidly moving crystalline front invading metastable liquid.

Acknowledgements

We thank Zhi-Feng Huang for useful suggestions and valuable discussions on the manuscript. P. K. G. acknowledges the partial support of the Russian Foundation for Basic Research (RFBR Project No. 14-29-10282ofi-m). P. K. G. is also grateful for support from the Administration of the Physical Faculty during his stay in Oakland University (Rochester, MI). K. R. E. and F. I. S. acknowledge support from the NSF under Grant No. DMR-0906676.

[1]Here: FCC is a face centered cubic, BCC is a body centered cubic, and HCP is a hexagonal close packed crystal lattices.

References

[1] S. M. Allen, J. W. Cahn, A microscopic theory for antiphase boundary motion and its application to antiphase domain coarsening, Acta Metall. 27 (1979) 1085-1095.

[2] P. Pelcé, Dynamics of Curved Fronts, Academic, Boston, 1988.

[3] M. C. Cross, P. C. Hohenberg, Pattern formation outside of equilibrium, Rev. Mod. Phys. 65 (1993) 851-1112.

[4] W. van Saarlos, Front propagation into unstable states, Phys. Rep. 386 (2003) 29-222.

[5] A. R. Deshpande, H. Xu, J. M. K. Wiezorek, Effect of grain size on coercivity of combined reaction processed FePd intermetallics, Acta Mater. 52 (2004) 2903-2911.

[6] P. K. Galenko, K. R. Elder, Marginal stablity analysis of the phase field crystal model in one spatial dimension, Phys. Rev. B 83 (2011) 064113-1-8.

[7] K. R. Elder, M. Katakowski, M. Haataja, M. Grant, Modeling Elasticity in Crystal Growth, Phys. Rev. Lett. 88 (2002) 245701-1-4.

[8] K. R. Elder, M. Grant, Modeling elastic and plastic deformations in nonequilibrium processing using phase field crystals, Phys. Rev. E 70 (2004) 051605-1-18.

[9] K. R. Elder, N. Provatas, J. Berry, P. Stefanovich, M. Grant, Phase-field crystal modeling and classical density functional theory of freezing, Phys. Rev. B 75 (2007) 064107-1-14.

[10] N. Provatas, K. Elder, Phase-Field Methods in Materials Science and Engineering, Wiley-VCH, Weinheim, 2010.

[11] K. R. Elder, G. Rossi, P. Kanerva, F. Sanches, S.-C. Ying, E. Granato, C. V. Achim, T. Ala-Nissila, Patterning of heteroepitaxial overlayers from nano to micron scales, Phys. Rev. Lett. 108 (2012) 226102-1-5.

[12] H. Emmerich, H. Löwen, R. Wittkowski, T. Gruhn, G. I. Toth, G. Tegze, L. Gránásy, Phase-field-crystal models for condensed matter dynamics on atomic length and diffusive time scales: an overview, Advances in Physics 61 (2012) 665-743.

[13] P. K. Galenko, H. Gomez, N. V. Kropotin, K. R. Elder, Unconditionally stable method and numerical solution of the hyperbolic phase-field crystal equation, Phys. Rev. E 88 (2013) 013310-1-11.

[14] N. Goldenfeld, B. P. Athreya, J. A. Danzig, Renormalization group approach to multiscale simulation of polycrystalline materials using the phase field crystal model, Phys. Rev. E 72 (2005) 020601(R)-1-4.

[15] B. P. Athreya, N. Goldenfeld, J. A. Danzig, Renormalization-group theory for the phase-field crystal equation, Phys. Rev. E 74 (2006) 011601-1-13.

[16] Z.-F. Huang, Scale-coupling and interface-pinning effects in the phase-field-crystal model, Phys. Rev. E 87 (2013) 012401-1-14.

[17] P. Galenko, D. Danilov, V. Lebedev, Phase-field-crystal and Swift-Hohenberg equations with fast dynamics, Phys. Rev. E 79 (2009) 0511101-1-11.

[18] K.-A. Wu, A. Karma, Phase-field crystal modeling of equilibrium bcc-liquid interfaces, Phys. Rev. B 76 (2007) 1841071-1-10.

[19] A. Jaatinen, C. V. Achim, K. R. Elder, T. Ala-Nissila, Thermodynamics of bcc metals in phase-field-crystal models, Phys. Rev. E 80 (2010) 031602-1-10.

[20] K. R. Elder, Zh.-F. Huang, N. Provatas, Amplitude expansion of the binary phase-field-crystal model, Phys. Rev. E 81 (2010) 011602-1-11.

[21] Zh.-F. Huang, K. R. Elder, N. Provatas, Phase-field-crystal dynamics for binary systems: Derivation from dynamical density functional theory, amplitude equation formalism, and applications to alloy heterostructures, Phys. Rev. E 82 (2010) 021605-1-22.

[22] P. Galenko, D. Jou, Diffuse-interface model for rapid phase transformations in nonequilibrium systems, Phys. Rev. E 71 (2005) 046125-1-13.

[23] J. A. P. Ramos, E. Granato, S. C. Ying, C. V. Achim, K. R. Elder, T. Ala-Nissila, Dynamical transitions and sliding friction of the phase-field-crystal model with pinning, Phys. Rev. E 81 (2010) 011121-1-7.

[24] V. Lebedev, A. Sysoeva, P. K. Galenko, Unconditionally gradient-stable computational schemes in problems of fast phase transitions, Phys. Rev. E 83 (2011) 026705-1-11.

[25] P. Stefanovic, M. Haataja, N. Provatas, Phase-Field Crystals with Elastic Interactions, Phys. Rev. Lett. 96 (2006) 225504-1-4.

[26] P. Stefanovic, M. Haataja, N. Provatas, Phase field crystal study of deformation and plasticity in nanocrystalline materials, Phys. Rev. E 80 (2009) 046107-1-10.

[27] A. J. Archer, Dynamical density functional theory for molecular and colloidal fluids: A microscopic approach to fluid mechanics, J. Chem. Phys. 130 (2009) 014509-1-8.

[28] N. W. Ashcroft and N. D. Mermin, Solid State Physics, Brooks Cole, 10 Davis Drive, Belmont, CA, 1976.

[29] Zh.-F. Huang, K. R. Elder, Morphological instability, evolution, and scaling in strained epitaxial films: An amplitude-equation analysis of the phase-field-crystal model, Phys. Rev. B 81 (2010) 165421-1-12.

[30] P. K. Galenko, D. A. Danilov, Hyperbolic self-consistent problem of heat transfer in rapid solidification of supercooled liquid, Phys. Lett. A 278 (2000) 129-138.

[31] P.K. Galenko, D.A. Danilov, Local-nonequilibrium effect on rapid dendritic growth in a binary alloy melt, Phys. Lett. A 235 (1997) 271-280.

[32] P.K. Galenko, D.A. Danilov, Model for free dendritic alloy growth under interfacial and bulk phase nonequilibrium conditions, J. Cryst. Growth 197 (1999) 992-1002.

[33] H. Humadi, J. J. Hoyt, N. Provatas, Phase-field-crystal study of solute trapping, Phys. Rev. E 87 (2013) 022404-1-10.

[34] P. K. Galenko, E. V. Abramova, D. Jou, D. A. Danilov, V. G. Lebedev, D. M. Herlach, Solute trapping in rapid solidification of a binary dilute system: A phase-field study, Phys. Rev. E 48 (2011) 041143-1-17.

[35] H. Hartmann, D. Holland-Moritz, P. K. Galenko, D. M. Herlach, Evidence of the transition from ordered to disordered growth during rapid solidification of an intermetallic phase, Europhysics Letters 87 (2009) 40007-1-6.

[36] P. K. Galenko, Extended thermodynamical analysis of a motion of the solid-liquid interface in a rapidly solidifying alloy, Phys. Rev. B 65 (2002) 144103-1-11.

[37] P. K. Galenko, Rapid advancing of the solid-liquid interface in undercooled alloys, Mater. Sci. Eng. A 375-377 (2004) 493-497.

[38] Y. Oono, S. Puri, Study of phase-separation dynamics by use of cell dynamical systems. I. Modeling, Phys. Rev. A 38 (1988) 434-453.

[39] P. K. Galenko, M. D. Krivilyov, Modelling of crystal pattern formation in isothermal undercooled alloys, Modelling Simul. Mater. Sci. Eng. 8 (2000) 8194.

[40] P. J. Roache, Computational Fluid Dynamics, Hermosa, Albuquerque, NM, 1976.

[41] D. Dobson, Self diffusion in liquid iron, in: Annual Report 2000 of Bayerisches Geoinstitut, University of Bayreuth, Bayreuth, 2000, p. 3.5b.

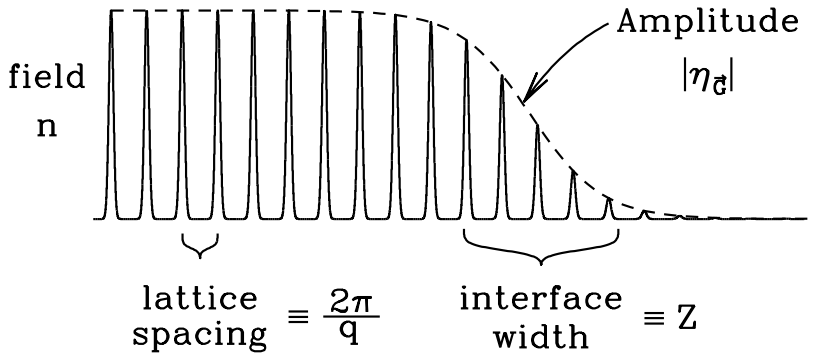

Figure 1: Spatial distribution of the field n near a liquid-solid interface, where peaks in n correspond to average atomic positions. The envelope of these peaks is described by the amplitude η of the n field (shown by dashed line). The interface width Z represents the transition region between atomically homogeneous and periodic states. Atomic positions in the lattice have the distance $a_0 = 2\pi/q$ with q the wave-number.

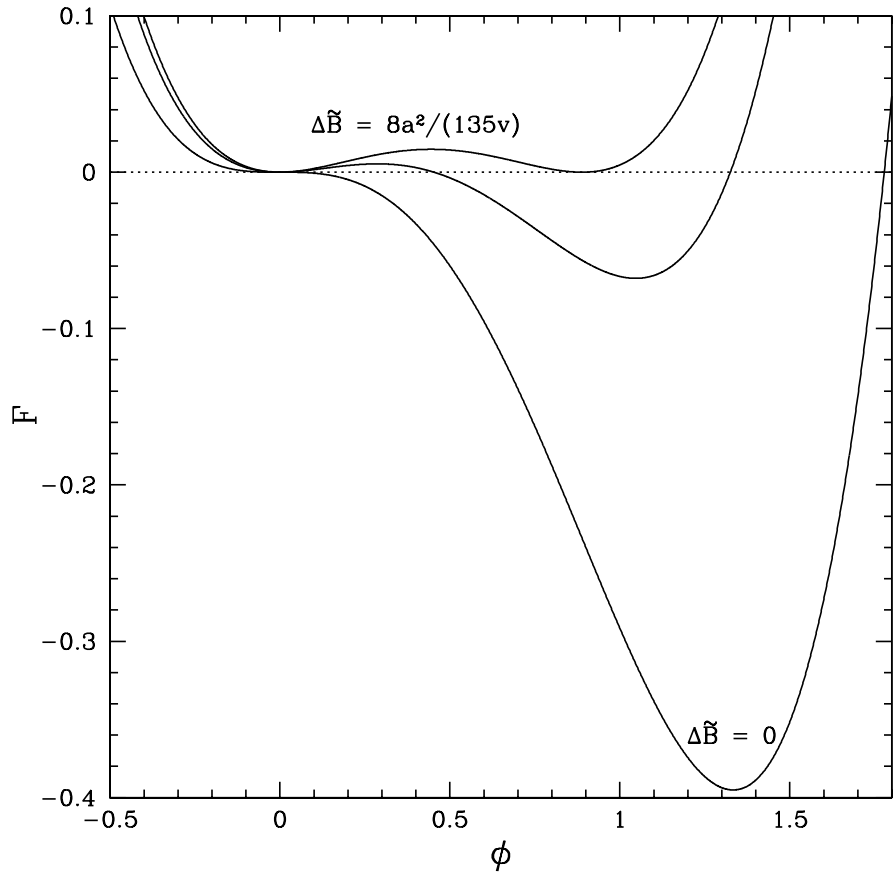

Figure 2: Free energy density for the spatially homogeneous system, for parameters $B_0^x = a = 1$ and $v = 0.1$.

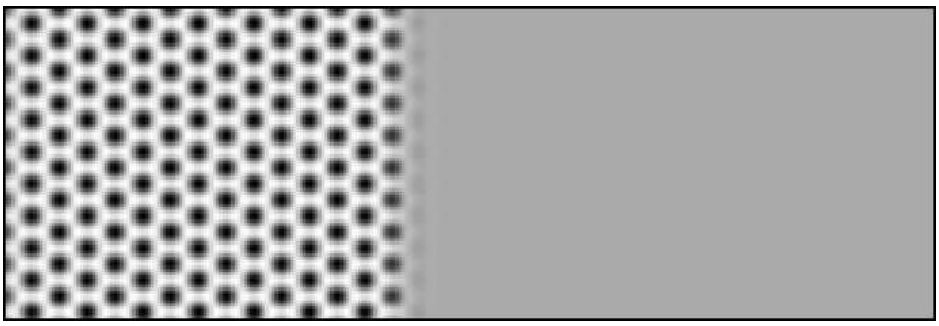

Figure 3: Two-dimensional sample front between solid (shown by the periodic triangular pattern, left) and liquid (shown as the homogeneous pattern, right). Petterns and diffuse front are obtained from reconstruction of the amplitudes simulated with Eq. (9) for the parameters $B_0^x = a = 1$, $v = 0.1$ and $\Delta B_0 = \Delta B_0^*$.

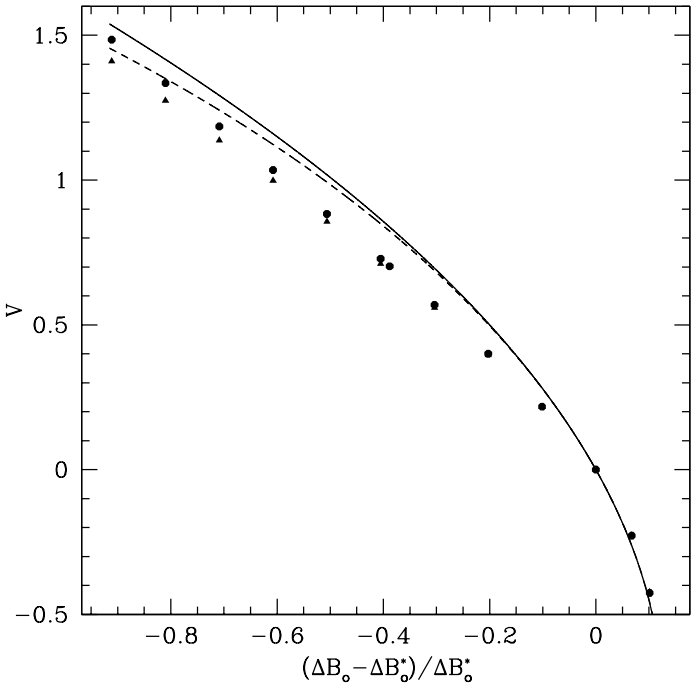

Figure 4: Front velocity V as a function of driving force $(\Delta B_0 - \Delta B_0^*)/\Delta B_0^*$. The lines from top to bottom correspond to the analytic calculations by Eq. (31) together with Eq. (27) for $\tau = 0$ and 0.1, respectively, and for a given equilibrium value of the wavenumber $q = q_e = 1$. The solid circles and triangles correspond to the velocity obtained in numerical solution of the amplitude equation (9) expanded as Eqs. (9) for $\tau = 0$ and 0.1, respectively.

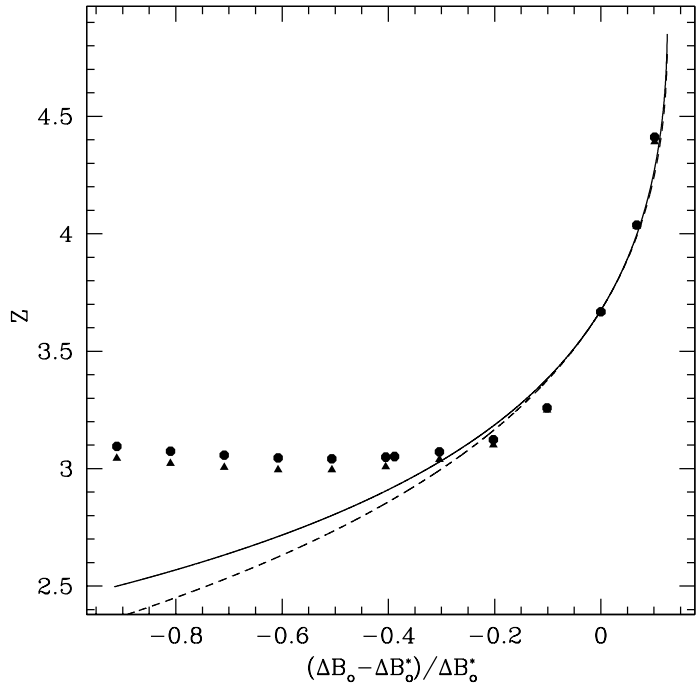

Figure 5: Interfacial width (correlation length) Z as a function of driving force $(\Delta B_0 - \Delta B_0^*)/\Delta B_0^*$. The lines from top to bottom correspond to analytic calculations by Eq. (33) together with Eqs. (27) and (32) for $\tau = 0$ and 0.1, respectively, and for a given equilibrium value of the wave-number $q = q_e = 1$. The solid circles and triangles correspond to numerical results obtained in simulations of the amplitude expansions (9) for $\tau = 0$ and 0.1, respectively.

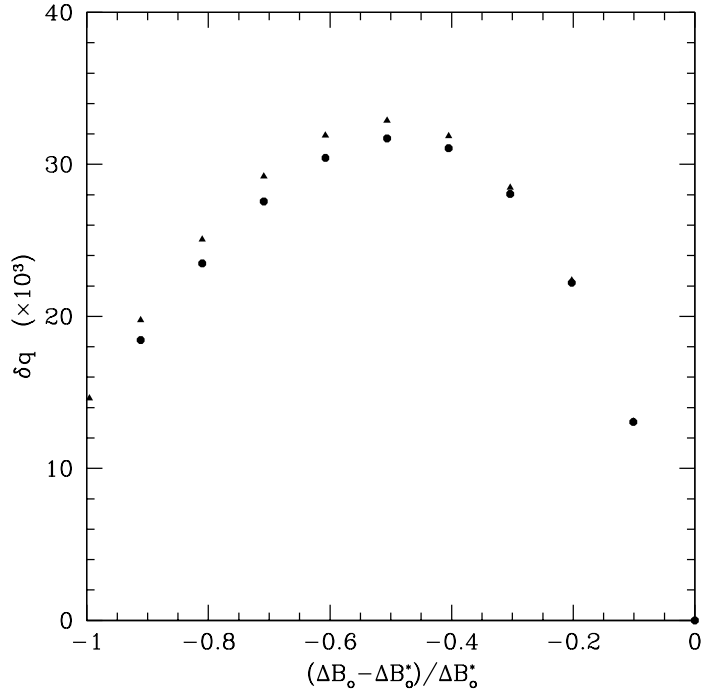

Figure 6: Wave-number $\delta q = q - q_e$ selected on the front of the PFC-pattern invading metastable homogeneous liquid. Here: $q \equiv |\vec{G}_j|$ and $q_e \equiv |\vec{G}^e_j|$. The solid circles and triangles correspond to results extracted from numerical simulations of the amplitude expansions (9) for $\tau = 0$ and 0.1, respectively.

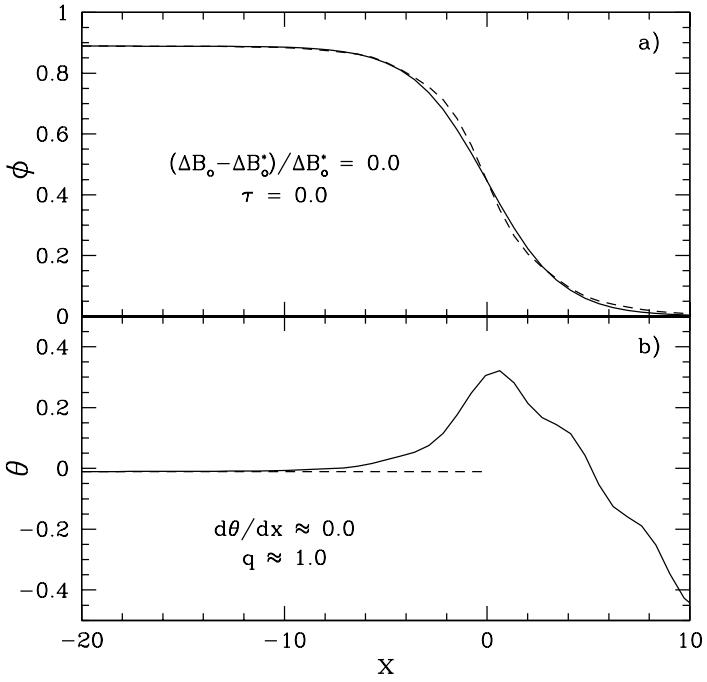

Figure 7: (a) Analytical scalar amplitude $\phi = \psi\phi_0$ given by solution (28) together with Eqs. (30)-(33) [solid line] in comparison with that numerically calculated from the amplitude equation (31) [dashed line]. Comparison is made for $(\Delta B_0 - \Delta B_0^*)/\Delta B_0^*$=0 and $\tau = 0$. (b) Behavior of the phase θ of complex amplitude (solid line) and a fit to a straight line (dashed line) are shown.

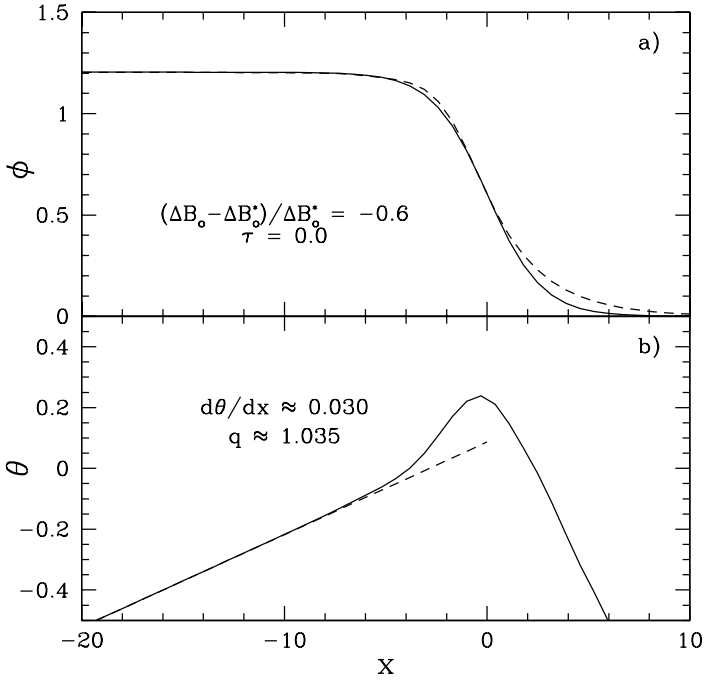

Figure 8: (a) Analytical scalar amplitude $\phi = \psi\phi_0$ given by solution (28) together with Eqs. (30)-(33) [solid line] in comparison with that numerically calculated from the amplitude equation (31) [dashed line]. Comparison is made for $(\Delta B_0 - \Delta B_0^*)/\Delta B_0^*$=-0.6 and $\tau = 0$. (b) Behavior of the phase θ of complex amplitude (solid line) and a fit to a straight line (dashed line) are shown.

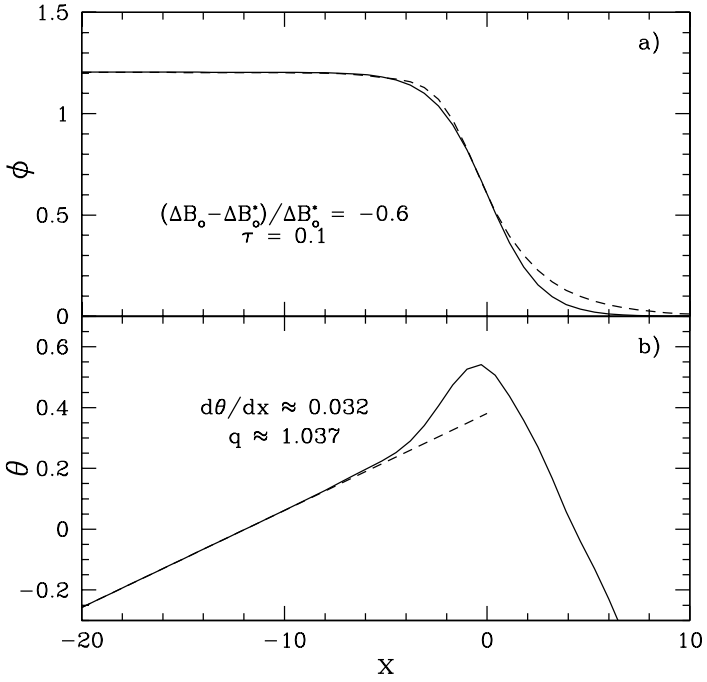

Figure 9: (a) Analytical scalar amplitude $\phi = \psi\phi_0$ given by solution (28) together with Eqs. (30)-(33) [solid line] in comparison with that numerically calculated from the amplitude equation (31) [dashed line]. Comparison is made for $(\Delta B_0 - \Delta B_0^*)/\Delta B_0^*$=-0.6 and $\tau = 0.1$. (b) Behavior of the phase θ of complex amplitude (solid line) and a fit to a straight line (dashed line) are shown.

Appendix A. Amplitude wave representation

The amplitude equations used in this manuscript can be obtained following the method of Goldenfeld et al. [14]. The procedure is:
(*i*) substitute the density wave profile (7) into equation of motion (6);
(*ii*) multiply by $\exp(i\vec{G}_j\vec{r})$ and integrate using "quick and dirty" approximation to obtain an amplitude equation;
(*iii*) retaining only the lowest order modes to obtain amplitude equation for η_1, η_2 and η_3. The "quick and dirty" approximation assumes that when integrating over a unit cell the amplitudes are constant.

Now, substituting the density wave profile (7) into equation of motion (6) gives the Laplacian in Eq. (3) as

$$\nabla^2 n = \vec{\nabla}\cdot\left[\sum_{j=1}^{3}\left(\vec{\nabla}\eta_j + i\vec{G}_j\eta_j\right)e^{i\vec{G}_j\cdot\vec{r}} + c.c.\right],$$

$$\nabla^2 n = \sum_{j=3}^{3}\left(\Lambda_j\eta_j e^{i\vec{G}_j\cdot\vec{r}} + c.c.\right), \tag{A.1}$$

with the operator

$$\Lambda_j = \nabla^2 + 2i\vec{G}_j\cdot\vec{\nabla} - G_j^2, \tag{A.2}$$

and with the summation over integers l, m, and n of the vector $\vec{G}_j$ given by Eq. (8). Typically, the magnitude of the vectors are chosen to correspond to the equilibrium values of the lattice constant [20, 21], i.e., $|\vec{G}_j| = q \equiv 1$. However, when a periodic front propagates into meta(un)stable phase, the wave number that is selected may not correspond to the equilibrium value [6]. For this reason it is convenient to expand around an arbitrary magnitude (see Ref. [11] and supplemental materials for it), i.e., $|\vec{G}_j| = q$.

Applying the procedure described above leads to the following equation of motion for the amplitudes,

$$\begin{aligned}\left(\tau\frac{\partial^2}{\partial t^2} + \frac{\partial}{\partial t}\right)\eta_j &= \Lambda_j\left[\left(\Delta B_0 + B_0^x\mathcal{G}_j^2\right)\eta_j + 2a\prod_{m\neq j}\eta_m^*\right.\\ &\quad\left. -3v\left(A_\eta^2 - |\eta_j|^2\right)\eta_j\right],\end{aligned} \tag{A.3}$$

where $A_\eta^2 = 2\sum_{j=1}^{3}|\eta_j|^2$ and $\mathcal{G}_j \equiv \nabla^2 + 2i\vec{G}_j\cdot\vec{\nabla} + 1 - q^2$. Finally, it is often assumed that the factor Λ_j can be replaced by $-q^2$ in the long wavelength

limit, since amplitudes are uniform in the equilibrium states. In this limit, Eq. (A.3) can be rewritten as

$$\left(\tau' \frac{\partial^2}{\partial t'^2} + \frac{\partial}{\partial t'}\right) \eta_j = -\Bigg[\left(\Delta B_0 + B_0^x \mathcal{G}_j^2\right) \eta_j + 2a \prod_{m \neq j} \eta_m^* - 3v \left(A_\eta^2 - |\eta_j|^2\right) \eta_j\Bigg], \tag{A.4}$$

where $\tau' \equiv q^2 \tau$ and $t' \equiv q^2 t$. For convenience, the prime will be dropped in the main sections of the manuscript.

Appendix B. Numerical approximation for the amplitude equations

In the case of the triangular lattice (see Sec. 3), the reciprocal lattice vectors are written as

$$\vec{G}_1 = \left[-\frac{\sqrt{3}}{2}, -\frac{1}{2}\right], \quad \vec{G}_2 = \left[\frac{\sqrt{3}}{2}, -\frac{1}{2}\right], \quad \vec{G}_3 = [0, 1]. \tag{B.1}$$

The three corresponding amplitude equations, described by Eq. (9) were solved numerically, using Euler's method for the time derivatives and "spherical" laplacian approximation [38] for the Laplacian operators, i..e,

$$\nabla^2 \eta_j \approx \frac{1}{\Delta x^2} \left(\frac{1}{2} \sum_n \eta_j + \frac{1}{4} \sum_{nn} \eta_j - 3\eta_j\right), \tag{B.2}$$

where $\sum_n$ and $\sum_{nn}$ represent sums over nearest and next nearest neighbours respectively. The single spatial derivatives were obtained with the following approximation

$$\frac{\partial \eta_j}{\partial x} \approx \frac{1}{4\Delta x} \left[\sum_n^r \eta_j - \sum_n^p \eta_j + \frac{1}{2} \left(\sum_{nn}^r \eta_j - \sum_{nn}^p \eta_j)\right)\right], \tag{B.3}$$

where $\sum_n^r$ and $\sum_n^p$ are sums over nearest neighbour to the right and left respectively and $\sum_{nn}^r$ and $\sum_{nn}^p$ are sums over next-nearest neighbour to right and left, respectively.

Additionally, a special stability condition of the proposed numerical algorithm were used. The two-dimensional hyperbolic equation with the second-order spatial derivatives has the stable numerical scheme as $\Delta t < (\Delta x)^2/8$

(see details in Ref. [39] for the scheme obtained by the Euler's method). In the present work, the fourth order spatial derivatives are used in the hyperbolic equation that should change the order of spatial accuracy in the criterion of stability condition. Therefore, one can derive that the present algorithm is linearly stable for the hyperbolic equation if the condition $\Delta t < (\Delta x)^4/8$ is met. Note that this condition is obtained as the necessary condition of numerical stability by von Neumann [40].

Appendix C. Estimations for relaxation times

In this appendix the value of the parameter τ is estimated, or more importantly the ratio τ/t_0 which appears in Eq. (24). ¿From Eq. (22) and Eq. (27) this ratio can be written as

$$\frac{\tau}{t_0} = \tilde{V}_\phi^{-2} = \frac{2q^2 B_0^x \Delta\tilde{B}_0}{V_\phi^2}, \tag{C.1}$$

with $\Delta\tilde{B}_0$ given by Eq. (17). In the dimensionless PFC model the length scales have all be scaled by the lattice constant and the time scales by the vacancy diffusion time. Thus the maximum dimensionless velocity V_ϕ has been scaled by a "diffusion" velocity given by $V^{(dif)} = D(T)/a_0$, where a_0 is the atomic spacing and $D(T)$ is the temperature dependent diffusion coefficient. Thus $V_\phi = V_\phi^{(dim)}/V^{(dif)}$, where $V_\phi^{(dim)}$ is maximum velocity in dimensional units (i.e., m/s).

To estimate $V^{(dif)}$ it is useful to note that the diffusion coefficient $D(T)$ is given by the Arrenius expression

$$D(T) = D_0 \exp\left[-Q_d/(R_g T)\right], \tag{C.2}$$

where R_g the gas constant, D_0 is the pre-factor, and Q_d the activation energy for the vacancy (defect) diffusion. For a concrete numerical estimation, let us consider a supercooled liquid Fe solidifying into a high-temperature BCC state. In the solidification process, we further assume that the front of the BCC-Fe invading liquid Fe will be dependent mainly on diffusion in the liquid phase just ahead of the front. In this instance experimental parameters for liquid iron are [41]: $D_0 = 6.4 \cdot 10^{-6}$ (m^2/s), $Q_d = 92.1$ (kJ/mole), and $R_g = 8.3$ (J/(mole·K)). For these parameters and the Arrenius law (C.2), the diffusion speed of defects around the propagating solid-liquid front is

estimated as $V^{(dif)} = D(T)/a_0 = 43.09$ (m/s) at $T = 1772$ (K), where $a_0 = 2.863 \cdot 10^{-10}$ (m). Taking the maximum speed $V_\phi^{(dim)} = 6 \cdot 10^2$ (m/s), the dimensionless speed of disturbances propagation is $V_\phi = V_\phi^{(dim)}/V^{(dif)} = 13.92$.

Now, taking into account the data from Ref. [18, 19], we use $q = 1.02$, $\Delta B_0^x = 0.332$, and $B_0^x = 11.583$ for $T = 1772$ (K) and an average number density of 0.0801 Å^{-3}. As a result, using all above estimations and Eq. (C.1), one obtains: $\tau/t_0 = 0.124$ and $\tau = 0.015$.

In the present estimate, the value of τ is small compared to unity. This is not a surprising result since the relaxation time τ is generally defined (in its dimensionless form) as the ratio between the relaxation time for the flux $\vec{J}$ and the relaxation time for ϕ. The flux $\vec{J}$ should relax to steady state faster than the relaxation of the ϕ-field, therefore, the relaxation time τ should be smaller unity. Therefore, at the estimated value $\tau \approx 10^{-2}$, a difference between parabolic and hyperbolic description of crystallization phenomena can be seen at very high values of the front velocity and large values of the driving force [30]. By this reason, finally, we specially note that numerical difference in present predictions of equations with $\tau = 0$ and $\tau = 0.1$ should not be so large in a pure (chemically one-component) system. However, such difference in τ must be quite essential in description of a binary system (i.e., in chemically two component systems [31, 32]) for which the presently obtained solutions will be logically advanced.